Theoretical analysis of field emission from metallic nanostructures on Si(100) surfaces

2004 J. Phys.: Condens. Matter 16 4685

(http://iopscience.iop.org/0953-8984/16/26/004)

INSTITUTE OF PHYSICS PUBLISHING JOURNAL OF PHYSICS: CONDENSED MATTER

J. Phys.: Condens. Matter **16** (2004) 4685–4696 PII: S0953-8984(04)77416-0

Theoretical analysis of field emission from metallic nanostructures on Si(100) surfaces

Y Gohda[1] **and S Watanabe**

Department of Materials Engineering, The University of Tokyo, 7-3-1 Hongo, Bunkyo-ku, Tokyo 113-8656, Japan
and
CREST, Japan Science and Technology Agency, 4-1-8 Honcho, Kawaguchi, Saitama 332-0012, Japan

E-mail: gohda@cello.t.u-tokyo.ac.jp

Received 5 March 2004
Published 18 June 2004
Online at stacks.iop.org/JPhysCM/16/4685
doi:10.1088/0953-8984/16/26/004

Abstract

We have analysed effects of submonolayer aluminium adsorption on field emission from Si(100) surfaces using *ab initio* density functional calculations incorporating scattering states. We have clarified that the electron transfer from aluminium atoms to silicon atoms plays an important role in reducing the local barrier height in front of aluminium atoms, resulting in large emission current. We have also found that, when nanostructures having comparable minimum local barrier height are considered, the relative efficiency of field emission can be explained by the difference in the density of emission sites and the surface local density of states at the Fermi energy.

1. Introduction

Field emission [1] can provide cold electron sources with low energy consumption. In particular, nanostructures fabricated on silicon surfaces [2] are of great interest because of possibilities for the control of field emission properties on the nanoscale. As one kind of such nanostructures, metal coating on silicon surfaces has been studied recently to improve the emission efficiency and the emission stability of silicon surfaces [3–5]. However, optimum conditions for field emission from metal-adsorbed silicon surfaces have not been clarified yet, although the coverage optimum for the emission efficiency is speculated to be the submonolayer regime for the flat plate configuration [3]. In another work of ours [6], field emission from the Si(100)2 × 2–Al surface which has an Al coverage of 0.5 monolayer (ML) has been compared with that from a clean silicon surface of an ultrathin film. We have pointed out that the local

[1] Present address: Physik-Department T30g, Technische Universität München, James-Franck-Straße, D-85747 Garching, Germany.

barrier height is more important than the work function as a key to understand the difference between the field emission properties. However, the origin of behaviours of the local barrier height has not been obtained, and, in this sense, the mechanism of the large emission current has not been clarified yet. One promising approach to clarify the mechanism is to compare among different materials with almost the same atomic structures, such as the comparison of single-atom terminated protrusions of almost the same size changing the material of substrates. Since the potential barrier is strongly affected by the electron distribution, it is helpful to estimate the Mulliken charge of each atom. Furthermore, although the minimum local barrier height has been found to be a key factor to understand the field emission properties from the analysis of the Si(100)2×2–Al surface, it is worth exploring other helpful factors to understand field emission from metallic nanostructures on silicon surfaces. Since metal-adsorbed silicon surfaces used in field emission experiments are usually disordered, analysis of field emission from small clusters as adsorbates is desirable.

In the present work, we report the results of our theoretical analysis on effects of the configuration of aluminium atoms adsorbed on the Si(100) surface using *ab initio* density functional calculations incorporating scattering states [7, 8] together with density functional calculations using localized basis sets. We have found that the electron transfer from aluminium atoms to silicon atoms plays an important role in reducing the local barrier height in front of aluminium atoms which leads to large field emission current. We have also clarified that, in addition to the minimum local barrier height, the difference in the density of emission sites and the surface local density of states at the Fermi energy are helpful factors that describe the relative efficiency of field emission from metallic structures on Si(100) surfaces.

2. Computational scheme

The field emission current was calculated within the framework of the density functional theory (DFT) [9, 10] for zero-temperature cases. To analyse electron transport, we have already developed a method based on *ab initio* density functional calculations incorporating scattering states [7, 8] that have been applied so far to field emission [7, 8, 11, 12], transport through atomic wires [13], issues on scanning tunneling microscopy [14, 15], the capacitance of nanoscale structures [16], and the atomic vibration by the electric field [17], obtaining results of interest successfully. Since this method has been reported only briefly in the previous publications, we describe the detail of this method named the boundary-matching scattering-state density functional (BSDF) method that eliminates unknown transmission and reflection coefficients utilizing boundary conditions to solve the Kohn–Sham equation straightforwardly as boundary-value problems. In this section, the atomic units are used to describe formulae for convenience, i.e. $e^2 = \hbar = m = 4\pi\varepsilon_0 = 1$, where e is the elementary positive charge, $\hbar$ is the Planck constant, m is the electron mass, and ε_0 is the dielectric constant in the vacuum.

2.1. Model

Since the BSDF method is based on the DFT [9, 10], a fully quantum mechanical description of electronic states including electronic many-body effects can be achieved from the DFT ansatz without any adjustable parameters. Assuming that electronic wavefunctions keep their phase, i.e. electrons are coherent and inelastic scattering does not occur, current-carrying electronic states are calculated explicitly in the BSDF method. Once one-electron scattering states are obtained, electronic states are occupied up to the quasi-Fermi level. Effects of an electric field or a bias voltage are included in the boundary conditions of the Poisson equation. Finally, electronic states including scattering states are self-consistently determined as solutions to the Kohn–Sham equations of the DFT.

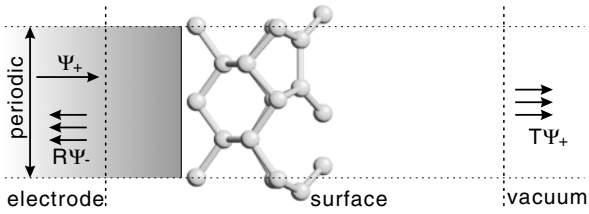

Figure 1. The model consists of a single semi-infinite electrode and the vacuum. The model is divided into three regions, and vertical dashed lines show the boundaries between adjacent regions.

In the present model, a single semi-infinite electrode is incorporated as an electron reservoir, because the BSDF method is applicable to field emission without a counterelectrode [7, 8, 11, 12, 17] as well as non-field-emission cases suitable for using two electrodes [13–16]. It should be emphasized that computation for field emission by the present method is remarkably efficient compared with conventional methods employing a counterelectrode, because the configuration of a counterelectrode makes the computational cost at least twice as high. Deep inside a semi-infinite electrode, ionic lattice cores are modelled by a uniform positive background charge called the jellium model. Although the jellium model is not indispensable in the present method, this model makes practical calculations considerably easier. To this semi-infinite jellium electrode, a nanostructure of interest is attached including the atomic structure explicitly. To incorporate translational symmetry of the surface, the periodic boundary conditions are imposed on the atomic arrangement of a nanostructure in the direction parallel to the surface.

The whole system represented by the model mentioned above is divided into the following three regions as shown in figure 1:

(i) the electrode region which is deep inside the jellium having a homogeneous one-electron effective potential and electronic states are described using plane waves,
(ii) the surface region which includes an ionic slab of a nanostructure and self-consistent DFT calculations are performed numerically, and
(iii) the vacuum region which is far from the surface and an electric field is regarded as nearly constant.

Here, we would like to comment on the model of flat surfaces used in our calculations. In most of the field-emission experiments, sharp needle structures have been used as field emitters, because local electric fields of the order of 2–10 V nm^{-1} are necessary on the apex of a field emitter. Since the typical radius of the apex is of the order of 100 nm, a surface of field emitters is practically flat on the atomic scale. Thus, in our work, the adopted model consists of flat surfaces with an applied local electric field F which includes effects of the field enhancement factor β.

Since electrons are emitted from an electrode to the vacuum in field emission, the emission process is considered as follows. First, electrons travel from the electrode region to the surface region as a plane wave $\exp(\mathrm{i}k_z)$. Next, electrons are elastically scattered at the surface region. Finally, the scattered electron wave is partially transmitted as a superposition of scattering waves $\sum_j T_j w^j(z)$ where $w^j(z)$ is a known function, and the rest of the wave is reflected as a superposition of plane waves $\sum_{m'} R_{m'} \exp(-\mathrm{i}k_z^{m'} z)$. To consider the process in this way means that electronic states are treated as nonequilibrium steady states. Transient phenomena are not considered, while they can be analysed by time-dependent methods [18, 19].

2.2. Solutions to the Kohn–Sham equations

Since it is essential to analyse electronic states as a scattering problem, the BSDF method eliminates unknown transmission and reflection coefficients utilizing boundary conditions, and solves the Kohn–Sham equation straightforwardly as boundary-value problems. In contrast to the conventional band structure calculations where the Kohn–Sham equation is solved as an eigenvalue problem for given $\boldsymbol{k}$, in the present method, $\boldsymbol{k}$ in the current-flow direction (z direction), k_z, cannot be a good quantum number in the scattering region because of the absence of periodicity in the z direction. Therefore, the Kohn–Sham equation is solved for a given energy E.

Imposing periodic boundary conditions in the direction parallel to the surface ($\boldsymbol{r}_\parallel$ direction), a one-electron wavefunction $\Psi_{E\boldsymbol{k}_\parallel}(\boldsymbol{r}_\parallel, z)$ and the effective potential $V_{\rm eff}(\boldsymbol{r}_\parallel, z)$ in the surface region are expanded by plane waves:

$$\Psi_{E\boldsymbol{k}_\parallel}(\boldsymbol{r}_\parallel, z) = \sum_j \psi(\boldsymbol{G}_\parallel^j, z)\mathrm{e}^{-\mathrm{i}(\boldsymbol{k}_\parallel+\boldsymbol{G}_\parallel^j)\cdot\boldsymbol{r}_\parallel}, \tag{1}$$

$$V_{\rm eff}(\boldsymbol{r}_\parallel, z) = \sum_j V_{\rm eff}(\boldsymbol{G}_\parallel^j, z)\mathrm{e}^{-\mathrm{i}\boldsymbol{G}_\parallel^j\cdot\boldsymbol{r}_\parallel}. \tag{2}$$

In practice, these Fourier expansions are truncated within j that satisfies $E_{\parallel,\rm cut} \geqslant |\boldsymbol{k}_\parallel+\boldsymbol{G}_\parallel^j|^2/2$. The accuracy of these truncated expansions can be controlled by adjusting the lateral cut-off energy $E_{\parallel,\rm cut}$. By using these Fourier components $\psi(\boldsymbol{G}_\parallel^j, z)$ and $V_{\rm eff}(\boldsymbol{G}_\parallel^j, z)$, the Kohn–Sham equation is reduced to a second-order ordinary differential equation:

$$\frac{1}{2}\frac{\mathrm{d}^2}{\mathrm{d}z^2}\psi^j(z) = \sum_{j'} V_{jj'}(z)\psi^{j'}(z). \tag{3}$$

Here, the definitions of symbols are as follows:

$$\psi^j(z) = \psi(\boldsymbol{G}_\parallel^j, z), \tag{4}$$

$$V_{jj'}(z) = V_{\rm eff}(\boldsymbol{G}_\parallel^j - \boldsymbol{G}_\parallel^{j'}, z) + \left[\tfrac{1}{2}|\boldsymbol{k}_\parallel + \boldsymbol{G}_\parallel^j|^2 - E\right]\delta_{jj'}, \tag{5}$$

where $\delta_{jj'}$ is the Kronecker delta.

This ordinary differential equation (3) is transformed into a set of difference equations by discretization in the z direction using the Noumerov method [20] and is expressed as coupled linear algebraic equations:

$$\sum_{j'}\left[\left(\delta_{jj'} - \frac{h^2}{6}V_{jj'}(z_{i-1})\right)\psi^{j'}(z_{i-1}) - \left(2\delta_{jj'} + \frac{5h^2}{3}V_{jj'}(z_i)\right)\psi^{j'}(z_i) + \left(\delta_{jj'} - \frac{h^2}{6}V_{jj'}(z_{i+1})\right)\psi^{j'}(z_{i+1})\right] = \mathrm{O}(h^6). \tag{6}$$

In the following, the most important point in the present numerical treatment is described: the removal of unknown transmission coefficients T_{jm} and reflection coefficients $R_{mm'}$ from boundary conditions.

2.2.1. Boundary condition inside the jellium electrode. First, the boundary condition deep inside the jellium is described. In a bulk jellium, electronic wavefunctions are given by plane waves. Therefore, deep inside the jellium, an electronic wavefunction consists of an incident plane wave and reflected plane waves:

$$\Psi_{E\boldsymbol{k}_\parallel m}(\boldsymbol{r}_\parallel, z) = \mathrm{e}^{\mathrm{i}k_z^m z}\mathrm{e}^{-\mathrm{i}(\boldsymbol{k}_\parallel+\boldsymbol{G}_\parallel^m)\cdot\boldsymbol{r}_\parallel} + \sum_{m'=1}^{M} R_{mm'}\mathrm{e}^{-\mathrm{i}k_z^{m'}z}\mathrm{e}^{-\mathrm{i}(\boldsymbol{k}_\parallel+\boldsymbol{G}_\parallel^{m'})\cdot\boldsymbol{r}_\parallel}, \tag{7}$$

where superscript m satisfies

$$\frac{|\boldsymbol{k}_\parallel + \boldsymbol{G}_\parallel^m|^2 + (k_z^m)^2}{2} = E. \tag{8}$$

Here, E is measured from the bottom of the jellium potential, and sampling of $\boldsymbol{k}_\parallel$ points is done in the surface Brillouin zone. Due to the uniformity of electronic states in the $\boldsymbol{r}_\parallel$ direction, a quantum number is specified by $\boldsymbol{k}_\parallel$ and m together with E. It should be noted that the size of the reflection matrix $\boldsymbol{R}$ is $M \times M$, where M is the number of m which satisfies equation (8). An m'th Fourier component of equation (7) satisfies the following relationships at the boundary $z = z_1$:

$$\psi_m^{m'}(z_1) = \mathrm{e}^{\mathrm{i}k_z^m z_1}\delta_{mm'} + R_{mm'}\mathrm{e}^{-\mathrm{i}k_z^{m'} z_1}, \tag{9}$$

$$\left.\frac{\mathrm{d}}{\mathrm{d}z}\psi_m^{m'}(z)\right|_{z=z_1} = \mathrm{i}k_z^m \mathrm{e}^{\mathrm{i}k_z^m z_1}\delta_{mm'} - \mathrm{i}k_z^{m'} R_{mm'}\mathrm{e}^{-\mathrm{i}k_z^{m'} z_1}. \tag{10}$$

Since $\mathrm{e}^{\mathrm{i}k_z^m z_1}$ represents the phase of an independent incident wave, $\mathrm{e}^{\mathrm{i}k_z^m z_1}$ is arbitrarily set to unity. In contrast to analytically solvable cases, we must remove unknown reflection coefficients $R_{mm'}$ from the boundary conditions. Combining the equation (9) with the equation (10), $R_{mm'}$ is eliminated, and, consequently, the boundary condition deep inside the jellium electrode is given as

$$\left.\frac{\mathrm{d}}{\mathrm{d}z}\psi_m^j(z)\right|_{z=z_1} = 2\mathrm{i}k_z^m\delta_{mj} - ik_z^{m'}\delta_{m'j}\psi_m^j(z_1). \tag{11}$$

Precisely speaking, in the present method, not only travelling plane waves but also evanescent waves which decay exponentially toward the inside of the electrode are included in the boundary condition as a Fourier component which has an apparent energy larger than E in the surface direction. It should be noted that wavefunctions growing exponentially toward the inside of the electrode are unphysical, and thus are excluded. For these evanescent waves, the boundary condition which is not written in equation (11) becomes as follows:

$$\left.\frac{\mathrm{d}}{\mathrm{d}z}\psi_m^\mu(z)\right|_{z=z_1} = \kappa_z^\mu\psi_m^\mu(z_1), \tag{12}$$

where $\kappa_z^\mu = \sqrt{|\boldsymbol{k}_\parallel + \boldsymbol{G}_\parallel^\mu|^2 - 2E}$. Here, μ is a Fourier component j for which no real k_z^j satisfies equation (8).

2.2.2. Boundary condition in the vacuum. Next, the boundary condition in the vacuum is described. In the vacuum region sufficiently far from the surface region, an electric field F can be regarded as constant, because the density of electrons and their interactions are negligibly small. In this situation, the effective potential is described as $V_{\mathrm{eff}}(\boldsymbol{r}) = V_{\mathrm{eff}}(z_{\mathrm{vac}}) - (z - z_{\mathrm{vac}})F$, where z_{vac} denotes a point in the vacuum region. In this region, the Schrödinger equation becomes

$$-\frac{1}{2}\frac{\mathrm{d}^2}{\mathrm{d}z^2}\psi_m^j(z) + \left[V_{\mathrm{eff}}(z_{\mathrm{vac}}) - (z - z_{\mathrm{vac}})F\right]\psi_m^j(z) = \left(E - \frac{|\boldsymbol{k}_\parallel + \boldsymbol{G}_\parallel^j|^2}{2}\right)\psi_m^j(z). \tag{13}$$

Since the Airy functions $\mathrm{Ai}(-\zeta)$ and $\mathrm{Bi}(-\zeta)$ are two independent solutions to the differential equation $y'' + \zeta y = 0$, the solutions to the equation (13) are $\mathrm{Ai}(-\zeta)$ and $\mathrm{Bi}(-\zeta)$, where

$$\zeta = (2F)^{1/3}\left[z - z_{\mathrm{vac}} - \frac{V_{\mathrm{eff}}(z_{\mathrm{vac}}) - E + \frac{1}{2}|\boldsymbol{k}_\parallel + \boldsymbol{G}_\parallel^j|^2}{F}\right]. \tag{14}$$

It should be emphasized that the Airy functions $\mathrm{Ai}(-\zeta)$ and $\mathrm{Bi}(-\zeta)$ cannot be adopted directly as a Fourier component of wavefunctions in the vacuum, because electronic states in the present consideration are scattering states. Thus a scattering wave $w(z)$ is constructed from $\mathrm{Ai}(-\zeta)$ and $\mathrm{Bi}(-\zeta)$ as

$$w(z) = C\big[\mathrm{Bi}(-\zeta) + \mathrm{iAi}(-\zeta)\big]. \tag{15}$$

This function $w(z)$ corresponds to a scattering state which propagates toward the $+z$ direction. Now, $w(z)$ and $w^*(z)$ are available as independent solutions instead of $\mathrm{Ai}(-\zeta)$ and $\mathrm{Bi}(-\zeta)$. Since the function $w^*(z)$ propagates toward the $-z$ direction, only $w(z)$ is necessary as a scattering wave in the vacuum region in the case of field emission. As for the constant C, it is determined using the current conservation condition. The current density calculated from equation (15) becomes

$$j_z = \mathrm{Im}\left[w^*(z)\frac{\mathrm{d}}{\mathrm{d}z}w(z)\right] = \frac{C^2(2F)^{1/3}}{\pi}. \tag{16}$$

Since the current density of a plane wave is $j_z = k_z$, it is convenient to define the normalization constant C as

$$C = \frac{\sqrt{\pi k_z^m}}{(2F)^{1/6}} \tag{17}$$

from the viewpoint of the current conservation law.

By using the propagating wave $w(z)$ defined in equations (15) and (17), a transmitted wave is expressed as

$$\Psi_{Ek_\parallel m}(\boldsymbol{r}_\parallel, z) = \sum_j T_{jm} w^j(z) \mathrm{e}^{-\mathrm{i}(\boldsymbol{k}_\parallel + \boldsymbol{G}_\parallel^j)\cdot \boldsymbol{r}_\parallel}. \tag{18}$$

Here, T_{jm} is one of the $N_G \times M$ components of the transmission matrix and N_G is the number of the surface reciprocal vectors $\boldsymbol{G}_\parallel^j$. At the boundary $z = z_N$, the continuation conditions of the wavefunction and its derivative are described as

$$\psi_m^j(z_N) = T_{jm} w^j(z_N), \tag{19}$$

$$\frac{\mathrm{d}}{\mathrm{d}z}\psi_m^j(z)\bigg|_{z=z_N} = T_{jm}\frac{\mathrm{d}}{\mathrm{d}z}w^j(z)\bigg|_{z=z_N}. \tag{20}$$

Consequently, the boundary condition in the vacuum is given by removing the transmission matrix T_{jm} as

$$\frac{\mathrm{d}}{\mathrm{d}z}\psi_m^j(z)\bigg|_{z=z_N} = \frac{\frac{\mathrm{d}}{\mathrm{d}z}w^j(z)|_{z=z_N}}{w^j(z_N)}\psi_m^j(z_N). \tag{21}$$

The boundary condition for transmitted waves in the case of the presence of a counterelectrode is derived replacing the Airy functions with plane waves.

These two numerically treatable boundary conditions (11) and (21) are effectively discretized by the Noumerov method [20]. By using the obtained algebraic form of the boundary conditions, the set of coupled linear equations (6) becomes a closed form, and numerical solutions to the Kohn–Sham equations satisfying the boundary conditions are obtained. After the wavefunction $\psi_m^j(z)$ is obtained, T_{jm} is calculated using equation (19). As shown here, this algorithm solves scattering problems without any complicated techniques such as those using the Green function and the transfer matrix. This simple idea of eliminating unknown transmission and reflection coefficients has already been applied to one-electron scattering problems [21]. We combined the idea with the DFT.

2.3. Electron density and current density

Wavefunctions obtained in the BSDF method are transformed into the real-space representation. Then the electron density is calculated from wavefunctions in real space. It should be noted that a Fourier grid for the electron density is set twice as dense as the grid for the wavefunction in each spatial direction [22].

Hereafter, the wavefunction $\Psi_{E\boldsymbol{k}_\parallel}(\boldsymbol{r})$ in equation (1) is rewritten as $\Psi_{E\boldsymbol{k}_\parallel m}(\boldsymbol{r})$ to specify its origin as the incident wave m. Since the set of E and $\boldsymbol{k}_\parallel$ is connected with $\boldsymbol{k}$ through the states of incident waves, we can use the wavevector of the incident wave defined in equation (8) as an alternative quantum number of $\Psi_{E\boldsymbol{k}_\parallel m}(\boldsymbol{r})$. The electron density $\rho(\boldsymbol{r})$ is calculated by performing integration in the k_z space and the surface Brillouin zone (sBZ) from states with infinitesimal energy to states with the Fermi energy E_F:

$$\rho(\boldsymbol{r}) = \frac{2}{(2\pi)^3}\sum_m \int_0^{\sqrt{2E_\mathrm{F}}} \mathrm{d}k_z^m \int^{\mathrm{sBZ}} \mathrm{d}\boldsymbol{k}_\parallel \, |\Psi_{E\boldsymbol{k}_\parallel m}(\boldsymbol{r})|^2. \tag{22}$$

Note that an incident wave m couples with the rest of the $(M-1)$ incident waves, M reflected waves, and N_G–M evanescent waves.

Since the Fermi surface of metals necessarily cuts at least one energy band and this band is partially occupied, computation of $\rho(\boldsymbol{r})$ using equation (22) is not straightforward. To calculate the electron density with the finite number of discrete $\boldsymbol{k}$ points, partially occupied quantum states have to be introduced near the Fermi surface in order to perform Brillouin-zone integration. For this purpose, we adopt the method of Methfessel and Paxton for Brillouin-zone integration [23–25] where the Heaviside function, i.e. the zero-temperature Fermi–Dirac distribution, is expanded in a complete orthogonal set of functions using the error function and the Hermite polynomials.

Due to an applied electric field, surface electronic states are in nonequilibrium. Therefore the Fermi surface has to be treated carefully [26]. Since electrons emit into the vacuum, the difference in the electron density of incident waves and reflected waves is

$$\rho_T = \frac{2}{(2\pi)^3}\sum_m \int_0^{\sqrt{2E_\mathrm{F}}} \mathrm{d}k_z^m \int^{\mathrm{sBZ}} \mathrm{d}\boldsymbol{k}_\parallel \sum_j T_{mj}^\dagger T_{jm}. \tag{23}$$

Therefore, the Fermi level has to be raised self-consistently to keep the charge neutrality deep in the jellium electrode as

$$E_\mathrm{F} = \tfrac{1}{2}\left[3\pi^2(\rho_+ + \rho_T)\right]^{2/3}, \tag{24}$$

where ρ_+ is the density of jellium. Here, we note that effects of space charges near the surface are included in the present method. Finally, the current density is calculated as

$$\boldsymbol{j}(\boldsymbol{r}) = \frac{2}{(2\pi)^3}\sum_m \int_0^{\sqrt{2E_\mathrm{F}}} \mathrm{d}k_z^m \int^{\mathrm{sBZ}} \mathrm{d}\boldsymbol{k}_\parallel \,\mathrm{Im}\left[\Psi^*_{E\boldsymbol{k}_\parallel m}(\boldsymbol{r})\nabla\Psi_{E\boldsymbol{k}_\parallel m}(\boldsymbol{r})\right]. \tag{25}$$

2.4. One-electron effective potential

The Hartree potential $V_\mathrm{H}(\boldsymbol{r})$ including effects of an external electric field is calculated by solving the Poisson equation in reciprocal space in the direction parallel to the surface. This potential includes the classical electrostatic part of electron–electron interactions, electron–jellium interactions, and effects of an external electric field. As for boundary conditions, the boundary condition deep inside the jellium electrode is given as the value of V_H, because V_H is constant in this region:

$$V_\mathrm{H}(\boldsymbol{G}_\parallel^j, z) = -\Big(V_\mathrm{XC}(\boldsymbol{G}_\parallel^j, z) + V_\mathrm{ion}(\boldsymbol{G}_\parallel^j, z)\Big)\delta_{\boldsymbol{G}_\parallel^j 0}. \tag{26}$$

The boundary condition in the vacuum is given as the differential of V_{H}, because an applied electric field F is approximately constant in the vacuum:

$$\frac{\mathrm{d}}{\mathrm{d}z}V_{\mathrm{H}}(\boldsymbol{G}_{\parallel}^{j},z)=\left(-\frac{\mathrm{d}}{\mathrm{d}z}V_{\mathrm{ion}}(\boldsymbol{G}_{\parallel}^{j},z)-F\right)\delta_{\boldsymbol{G}_{\parallel}^{j}0}. \tag{27}$$

It should be noted that, in this second boundary condition, the potential at the boundary in the direction parallel to the surface can be nonuniform in principle, although it becomes almost uniform if the boundary is sufficiently far from the surface.

Since the total charge is obtained as a calculated result, the convergence of transport calculations is extremely hard to achieve due to a change in the total charge in each iteration. To improve the convergence of the self-consistent potential, we employ the Lagrange multiplier method for the charge density in solving the Poisson equation.

In the framework of the DFT, all quantum mechanical many-body effects between electrons besides $V_{\mathrm{H}}(\boldsymbol{r})$ are included in the exchange–correlation potential $V_{\mathrm{XC}}(\boldsymbol{r})$. The present work adopts an exchange–correlation functional with the local density approximation [9, 10, 22] proposed by Ceperley and Alder, which is based on quantum Monte Carlo simulations of a homogeneous electron gas [27] and parametrized by Perdew and Zunger [28].

We employ pseudopotentials to exclude inert atomic core electrons from calculations. In the present work, local pseudopotentials [29, 30] are used. Due to the requirement of a relatively low cut-off energy, the use of these pseudopotentials remarkably reduces the computational cost compared with the case of nonlocal pseudopotentials. Calculations of the lattice constant and the total energy of the bulk silicon using this pseudopotential gave a satisfactory agreement with experiments [31].

3. Mulliken population analysis

In another analysis of ours [6], we have clarified that the Si(100)2 × 2–Al surface under a strong electric field has a small value of the minimum of the local barrier height (LBH), and the field emission current from this surface is much larger than that from clean silicon and aluminium surfaces. However, the mechanism of the large emission current has not been clarified yet. As an essential mechanism, we speculate the formation of local dipole moments caused by the charge transfer between silicon atoms and aluminium atoms.

To examine the validity of our speculation, we have analysed the Mulliken population of the aluminium adatoms of the Si(100)2 × 2–Al surface at 0.5 ML coverage by density functional calculations using localized basis sets and effective core potentials [27, 32–34]. A rectangular parallelepiped cluster used in the calculations is $Al_{24}Si_{269}H_{168}$ consisting of 12 pairs of aluminium ad-dimers, five 6 × 8-sized Si(100) planes, and hydrogen atoms to terminate the dangling bonds of silicon atoms. The atomic structure is the same as that used in our density functional transport calculations [6] except for the hydrogen terminations. For the two ad-dimers at the centre of the aluminium-adsorbed surface of the cluster, we have obtained the transfer of 0.22 electrons from each aluminium atom to silicon atoms. This result supports the formation of local dipole moments to reduce the local barrier height in front of the aluminium ad-dimers mentioned above. Consequently, the most essential mechanism of the large field emission current that is related to the local barrier height can be attributed to the electron transfer from Al atoms to Si atoms.

We have also calculated the Mulliken population of an aluminium-adsorbed surface that has clusters consisting of seven aluminium atoms analysed by our density functional transport calculations in the next section. This Al_7 cluster on the Si(100) surface is compared with an Al_{14} single-atom terminated protrusion on an Al(100) substrate analysed previously [8, 12]. We used

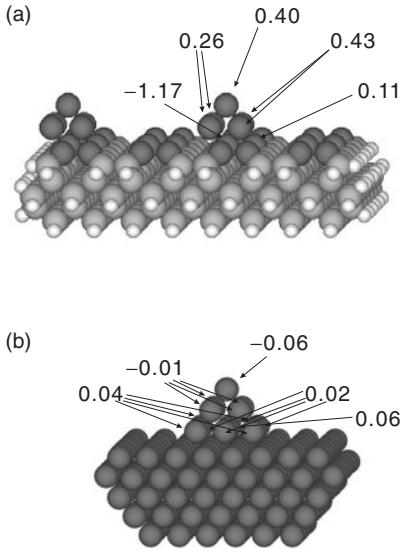

Figure 2. Models used in density functional calculations using localized basis sets and effective core potentials [27, 32–34] without the electric field: (a) an $Al_{34}Si_{269}H_{168}$ cluster and (b) an Al_{304} cluster. The Mulliken charges are shown for aluminium atoms consisting of protrusions.

density functional calculations using localized basis sets and effective core potentials [27, 32–34]. Figure 2(a) shows an model of the Al_7 cluster on the Si(100) surface, an $Al_{34}Si_{269}H_{168}$ cluster that includes two Al_7 clusters. As an model of an Al_{14} single-atom terminated protrusion on an Al(100) substrate, we used an Al_{304} cluster that has one Al_{14} protrusion as shown in figure 2(b). As for the model in figure 2(a), we direct our attention to only one of the Al_7 clusters that is closest to the centre of the aluminium-adsorbed Si(100) surface, because the other cluster is placed at the edge of the surface only to avoid the open-shell calculation that is computationally expensive. For the Al_7 cluster on the silicon surface, we have found that the topmost aluminium atom is positively charged by $0.40e$. This charging is caused by the transfer of 0.71 electrons from aluminium atoms to silicon atoms. In contrast, the apex atom of the Al_{14} single-atom terminated protrusion has a small negative charge of $-0.06e$. These results indicate that the decrease in the LBH for the Al_7 cluster on the Si(100) surface differs essentially from that for the single-atom terminated protrusion on the Al(100) surface. In the case of the single-atom terminated protrusion on the aluminium surface, the decrease in the LBH is mainly attributed to the image-potential effects [8, 12]. In contrast, in the case of the Al_7 cluster on the Si(100) surface, the electrostatic effects by the charging of the apex aluminium atom also play an important role.

4. Field emission from aluminium clusters

As an adsorption of aluminium atoms on the Si(100) surface, we have analysed the case where the coverage is slightly larger than 0.5 ML. In figure 3, we show the three models considered in the present analysis, i.e. Al_4, Al_6, and Al_7 clusters on the Si(100) surface of an ultrathin film. The Si(100) ultrathin film consisting of five silicon layers is attached to a semi-infinite jellium electrode. We configure aluminium atoms to form a part of the fcc lattice and set the bond length of aluminium atoms at its bulk value except for atoms directly contacting with silicon atoms. The height of the topmost aluminium atom measured from the height of the silicon dimers is 3.13 Å for Al_4 and Al_6 clusters, and is 5.16 Å for the Al_7 cluster. These values correspond well with those estimated from the experiment at 0.6 ML [35]. In the present analysis, field emission properties from each cluster on the Si(100) surface were calculated

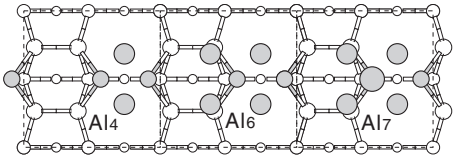

Figure 3. Models for Al_4, Al_6, and Al_7 clusters on a Si(100) surface of an ultrathin film. The dashed square is a two-dimensional unit cell with a periodicity of 2×2 used in the calculation and plots of the calculated results. Note that computations were performed for each cluster with the 2×2 periodicity. White circles indicate silicon atoms and grey circles indicate aluminium ones. The larger the size of the circles, the higher the atomic position among atoms of the same species. For silicon atoms, only the first three layers are shown.

Table 1. Minimum of the LBH measured from E_F, the number of emission sites N_s, and the field emission current density j for Si(100) surfaces. Applied external electric field F is 10 V nm^{-1}.

Structure	min (LBH) (eV)	N_s	j (nA nm^{-2})
Al_4 cluster	0.13	2	1900
Al_6 cluster	0.35	4	2000
Al_7 cluster	−0.54	1	4800
Clean	1.16	2	360
0.5 ML	0.17	2	1100

with the 2×2 periodicity. It should be noted that imposing this periodicity leads to much higher coverage than 0.6 ML. However, since we can expect to reproduce emission properties of each cluster reasonably well by the present model, we can estimate the emission properties of surfaces with realistic coverage of aluminium by considering the density of the aluminium clusters. It should also be noted that the shape of the aluminium clusters used in the present study is not optimized. However, such models of clusters are sufficient for the present purpose, that is, not to analyse the emission properties of metal-adsorbed silicon surfaces quantitatively in detail but to clarify dominant factors of their emission properties. In addition, detailed information on the atomic structure of such clusters is not available.

In table 1, we summarize calculated results of field emission properties for an applied electric field F of 10 V nm^{-1}. The order of the values of j is within the range obtained by the Stratton formula for field emission from semiconductors [36]. The value of j from the Al_7 cluster, 4800 nA nm^{-2}, is more than ten times as high as that from the clean Si(100) surface. In contrast, j from the Al_4 and Al_6 clusters are not so large as that from the Al_7 cluster. The large emission current from the Al_7 cluster is due to the small minimum of the LBH, −0.54 eV. As discussed in the previous section, the electron transfer from the apex aluminium atom to the substrate plays an essential role for the decrease in the LBH.

Comparing the Al_4 cluster with the Al_6 one, j from the Al_6 cluster is larger than that from the Al_4 cluster, although the minimum of the LBH of the Al_6 cluster, 0.35 eV, is slightly larger than that of the Al_4 cluster, 0.13 eV. This apparent discrepancy is explained by the number of emission sites N_s shown in table 1. We have confirmed that the minima of the LBH are located in front of the topmost atoms in all the cases we have studied. Since the Al_6 cluster has four topmost atoms, the number of emission sites of this cluster is twice the number of the sites of the Al_4 cluster. Since j is proportional to the number of emission sites, j from the Al_6 cluster becomes larger than that from the Al_4 cluster, in spite of the larger minimum LBH of the Al_6 cluster. It should be noted, however, that the number of emission sites is less important than the minimum LBH because of the exponential dependence of j on the minimum LBH.

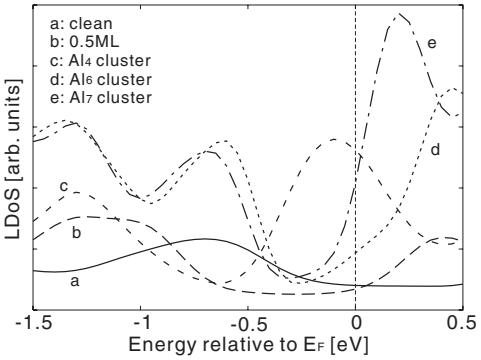

Figure 4. Surface LDoS integrated in the first silicon layer and in front of it in the case of $F = 10$ V nm^{-1}. For energies larger than E_F, electronic states are unoccupied.

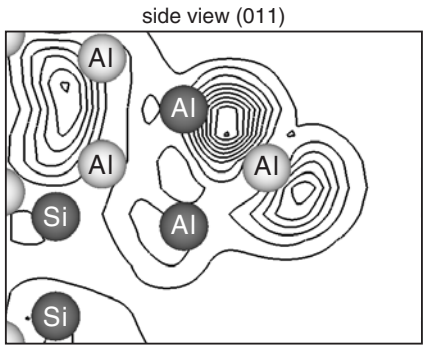

Figure 5. Distribution of electrons at E_F for the Al_7 cluster on the Si(100) surface in the case of $F = 10$ V nm^{-1}. The density is plotted in the vertical (011) plane containing the centre of ionic cores indicated by bright circles. Dark circles are ionic cores, the centre of which is out of the plane.

As seen in table 1, j from the Al_4 cluster (1900 nA nm^{-2}) is larger than that from the 0.5 ML adsorbed surface (1100 nA nm^{-2}), although the minimum of the LBH for the surface with the Al_4 clusters is almost the same as that for the 0.5 ML adsorbed surface. This increase in j can be explained by large local density of states (LDoS) at surfaces around E_F shown in figure 4. Here, the surface region includes the first silicon layer and adsorbed aluminium atoms together with the vacuum region containing space charges near the outermost layers. We can clearly see from this figure that the surface LDoS at E_F for the surface with the Al_4 cluster is the largest. Thus, the larger j from the Al_4 cluster than that from the 0.5 ML adsorbed surface can be attributed to the larger surface LDoS around E_F. This fact suggests that, if nanostructures having comparable minimum LBH are considered, the surface LDoS is a helpful factor to predict the field emission efficiency. It should be noted that j from the Al_7 cluster is also enhanced by the large surface LDoS. In this case, large amplitude of electronic states at E_F around the topmost aluminium atom, seen in the distribution of electrons at E_F shown in figure 5, reveals that a passage of emitted electrons through this atom exists.

As far as we have analysed, the field emission current increases monotonically as the size of adsorbates increases. However, the emission efficiency can decrease as the adsorbate coverage becomes much higher than the submonolayer regime analysed here, because the shape of a cluster often becomes smoother as its size becomes larger. Thus, we speculate that the optimum adsorbate coverage is not very high, which is consistent with an experiment [3].

5. Summary

We have analysed effects of metal adsorption on field emission from Si(100) surfaces using *ab initio* density functional calculations incorporating scattering states, where unknown transmission and reflection coefficients are eliminated utilizing boundary conditions, and the Kohn–Sham equation is solved straightforwardly as boundary-value problems. We have found that the electron transfer from aluminium atoms to silicon atoms plays an important role in reducing the local barrier height in front of aluminium atoms resulting in large emission current. We have also shown that relative efficiency of field emission can be explained by the difference in the density of emission sites and the surface local density of states at the Fermi energy when nanostructures having comparable minimum local barrier height are considered.

Acknowledgments

We gratefully acknowledge all the members in the CREST program headed by Professor H Fujita for stimulating discussions. Part of the numerical calculations were performed on Hitachi SR8000s at Institute for Solid State Physics, the University of Tokyo. One of us (YG) wishes to acknowledge the support from the Japanese Society for the Promotion of Science.

References

[1] Good R H and Müller E W 1956 *Handbuch der Physik* vol 21, ed S Flügge (Berlin: Springer) p 176
[2] Musa I, Munindrasdasa D A I, Amaratunga G A J and Eccleston W 1998 *Nature* **395** 362
[3] Wong W K, Meng F Y, Li Q, Au F C K, Bello I and Lee S T 2002 *Appl. Phys. Lett.* **80** 877 The value of the substantial coverages is much lower than the reported one, as is written in the literature
[4] Lee J L, Oh S P, Han S Y, Kang S Y, Lee J H and Cho K I 2000 *J. Appl. Phys.* **87** 7349
[5] Park H W, Ju B K, Lee Y H, Park J H and Oh M H 1996 *Japan. J. Appl. Phys.* **35** L1301
[6] Gohda Y and Watanabe S 2003 *J. Vac. Sci. Technol.* B **21** 2461
[7] Gohda Y, Nakamura Y, Watanabe K and Watanabe S 2000 *Phys. Rev. Lett.* **85** 1750
[8] Gohda Y and Watanabe S 2001 *Phys. Rev. Lett.* **87** 177601
[9] Hohenberg P and Kohn W 1964 *Phys. Rev.* **136** B864
[10] Kohn W and Sham L J 1965 *Phys. Rev.* A **140** 1133
[11] Gohda Y, Nakamura Y, Watanabe K and Watanabe S 2002 *Mater. Sci. Eng.* A **327** 1
[12] Gohda Y and Watanabe S 2002 *Surf. Sci.* **516** 265
[13] Furuya S, Gohda Y, Sasaki N and Watanabe S 2002 *Japan. J. Appl. Phys.* **41** L989
[14] Totsuka H, Gohda Y, Furuya S and Watanabe S 2002 *Japan. J. Appl. Phys.* **41** L1172
[15] Ando K, Bray-Ali N, Gohda Y and Watanabe S 2003 *Japan. J. Appl. Phys.* **42** 4642
[16] Tanaka M, Gohda Y, Furuya S and Watanabe S 2003 *Japan. J. Appl. Phys.* **42** L766
[17] Hu C P, Gohda Y, Furuya S and Watanabe S 2003 *Japan. J. Appl. Phys.* **42** 4639
[18] Han S, Lee M H and Ihm J 2002 *Phys. Rev.* B **65** 85405
[19] Tada K and Watanabe K 2002 *Phys. Rev. Lett.* **88** 127601
[20] Noumerov B V 1924 *Mon. Not. R. Astron. Soc.* **84** 592
[21] Lent C S and Kirkner D J 1990 *J. Appl. Phys.* **67** 6353
[22] Payne M C, Teter M P, Allan D C, Arias T A and Joannopoulos J D 1992 *Rev. Mod. Phys.* **64** 1045
[23] Methfessel M and Paxton A T 1989 *Phys. Rev.* B **40** 3616
[24] Kresse G and Furthmüller J 1996 *Phys. Rev.* B **54** 11169
[25] Kresse G and Furthmüller J 1996 *Comput. Mater. Sci.* **6** 15
[26] Lang N D 1992 *Phys. Rev.* B **45** 13599
[27] Ceperley D M and Alder B J 1980 *Phys. Rev. Lett.* **45** 566
[28] Perdew J P and Zunger A 1981 *Phys. Rev.* B **23** 5048
[29] Schlüter M, Chelikowsky J R, Louie S G and Cohen M L 1975 *Phys. Rev.* B **12** 4200
[30] Chelikowsky J R, Chadi D J and Cohen M L 1981 *Phys. Rev.* B **23** 4013
[31] Ihm J and Cohen M L 1979 *Solid State Commun.* **29** 711
[32] Frisch M J, Trucks G W, Schlegel H B, Scuseria G E, Robb M A, Cheeseman J R, Zakrzewski V G, Montgomery J A, Stratmann R E, Burant J C, Dapprich S, Millam J M, Daniels A D, Kudin K N, Strain M C, Farkas O, Tomasi J, Barone V, Cossi M, Cammi R, Mennucci B, Pomelli C, Adamo C, Clifford S, Ochterski J, Petersson G A, Ayala P Y, Cui Q, Morokuma K, Malick D K, Rabuck A D, Raghavachari K, Foresman J B, Cioslowski J, Ortiz J V, Baboul A G, Stefanov B B, Liu G, Liashenko A, Piskorz P, Komaromi I, Gomperts R, Martin R L, Fox D J, Keith T, Al-Laham M A, Peng C Y, Nanayakkara A, Challacombe M, Gill P M W, Johnson B, Chen W, Wong M W, Andres J L, Gonzalez C, Head-Gordon M, Replogle E S and Pople J A 1998 *Computer code Gaussian98 (Revision A.9)* (Pittsburgh, PA: Gaussian)
[33] Vosko S H, Wilk L and Nusair M 1980 *Can. J. Phys.* **58** 1200
[34] Stevens W, Basch H and Krauss J 1984 *J. Chem. Phys.* **81** 6026
[35] Nogami J, Baski A A and Quate C F 1991 *Phys. Rev.* B **44** R1415
[36] Stratton R 1962 *Phys. Rev.* **125** 67